TU Delft

Delft University of Technology

Convective Mass-Flux From Long Term Radar Reflectivities Over Darwin, Australia

Savazzi, Alessandro C.M.; Jakob, Christian; Siebesma, A. Pier

DOI
10.1029/2021JD034910

Publication date
2021

Document Version
Final published version

Published in
Journal of Geophysical Research: Atmospheres

Citation (APA)
Savazzi, A. C. M., Jakob, C., & Siebesma, A. P. (2021). Convective Mass-Flux From Long Term Radar Reflectivities Over Darwin, Australia. *Journal of Geophysical Research: Atmospheres*, *126*(19), Article e2021JD034910. https://doi.org/10.1029/2021JD034910

Important note
To cite this publication, please use the final published version (if applicable).
Please check the document version above.

Copyright
Other than for strictly personal use, it is not permitted to download, forward or distribute the text or part of it, without the consent of the author(s) and/or copyright holder(s), unless the work is under an open content license such as Creative Commons.

Takedown policy
Please contact us and provide details if you believe this document breaches copyrights.
We will remove access to the work immediately and investigate your claim.

This work is downloaded from Delft University of Technology.
For technical reasons the number of authors shown on this cover page is limited to a maximum of 10.

Check for updates

JGR Atmospheres

RESEARCH ARTICLE
10.1029/2021JD034910

Convective Mass-Flux From Long Term Radar Reflectivities Over Darwin, Australia

Alessandro C. M. Savazzi[1], Christian Jakob[2,3], and A. Pier Siebesma[1,4]

[1]Department of Geoscience and Remote Sensing, Delft University of Technology, Delft, Netherlands, [2]School of Earth, Atmosphere and Environment, Monash University, Melbourne, VIC, Australia, [3]ARC Centre of Excellence for Climate Extremes, Monash University, Melbourne, VIC, Australia, [4]Royal Netherlands Meteorological Institute (KNMI), De Bilt, Netherlands

Key Points:

- An observationally based data set of convective mass-flux spanning more than a decade is developed and analyzed
- The data set provides for the first time long-term observational estimates of net entrainment
- There is strong bulk entrainment in the lowest 4 km of the atmosphere and strong detrainment above that level

Correspondence to:
A. C. M. Savazzi,
A.C.M.Savazzi@tudelft.nl

Citation:
Savazzi, A. C. M., Jakob, C., & Siebesma, A. P. (2021). Convective mass-flux from long term radar reflectivities over Darwin, Australia. *Journal of Geophysical Research: Atmospheres*, *126*, e2021JD034910. https://doi.org/10.1029/2021JD034910

Received 17 MAR 2021
Accepted 9 SEP 2021

© 2021 The Authors.
This is an open access article under the terms of the Creative Commons Attribution-NonCommercial License, which permits use, distribution and reproduction in any medium, provided the original work is properly cited and is not used for commercial purposes.

Abstract Most cumulus parametrizations today make use of a simple conceptual model of convection, called the mass-flux approach. This approach depicts convection as an ensemble of updrafts and downdrafts occurring within a model grid-box. The aim of this study is to determine convective mass-fluxes and their constituents on the scale of a 100 km GCM grid-box from a C-band polarimetric radar and thereafter investigate the relative role of area fraction and vertical velocity in determining the shape and magnitude of bulk mass-flux profiles. We make use of observational estimates of these quantities spanning 13 wet seasons in the tropical region of Darwin. Following a bulk approach, the results show that the distribution of mass-flux is positively skewed and its mean profile peaks at 4 km. This is the result of constant area fractions and increasing vertical velocities below that level. Above 4 km, in-cloud vertical velocity plays a marginal role compared to the convective area fraction in controlling mass-flux profiles.

1. Introduction

It has long been recognized that deep convective systems play a key role in regulating the large-scale circulations and thermal structure of the atmosphere in the tropics (de Rooy et al., 2008; Emanuel et al., 1994; Labbouz et al., 2018; Riehl & Malkus, 1958, 1979; Simpson et al., 1998). Despite this, the underlying physical processes connected to convective clouds and their response to a warmer climate are not yet fully understood.

Cumulus convection is observed to organize into strong narrow updrafts which cover a small horizontal fraction of the large-scale atmosphere (e.g., Davies et al., 2013; Louf et al., 2019; Oerlemans, 1986). Because of the limited spatial resolution of General Circulation Models (GCMs), atmospheric convection occurs at a sub-grid scale and, thus, must be parameterized (Arakawa, 2004). As a result, progress in simulating clouds and precipitation in GCMs strongly relates to improvements in the cumulus cloud parameterizations and their coupling to boundary layer and cloud processes (e.g., Bechtold et al., 2008; Jakob, 2010).

Most cumulus parametrizations today make use of a simple conceptual model of convection, called the mass-flux approach (e.g., Arakawa et al., 1974; Ooyama, 1971; Tiedtke, 1989; Yanai et al., 1973). This approach depicts convection as an ensemble of updrafts and downdrafts occurring within a model grid-box. The area covered by the up- and downdrafts is assumed to be small compared to the grid-size. The mass-flux for an individual draft is defined as the product of the air density, the fractional area covered by the draft and the vertical velocity inside it. Most commonly, parametrizations apply the so-called bulk mass-flux approach (e.g., Gregory & Rowntree, 1990; Tiedtke, 1989), where only the average properties of the cloud ensemble are considered. The alternative spectral approach, where different cloud types are assumed to co-exist or even compete with each other (e.g., Arakawa et al., 1974; Wagner & Graf, 2010), while available, is less commonly used due to computational constraints. The essential assumption in either approach is that the vertical transport of any scalar is well represented by the product of the mass-flux and the bulk updraft scalar excess with respect to the updraft environment.

While conceptually simple, the evaluation of mass-flux approaches is challenging as it requires concurrent knowledge of the fractional area covered by convective clouds and the vertical velocity inside the clouds in domain of roughly 100 km at a side to match current global climate model resolutions. As a result, much of the evaluation and parameter estimation for mass-flux schemes has relied on the use of Cloud-Resolving

and Large-Eddy Simulation Models (e.g., de Rooy et al., 2008; Siebesma et al., 1996, 2020). These model experiments are often limited to short temporal extent and idealized atmospheric conditions. Furthermore, they show limits in reproducing convective organization and taking into account the large-scale conditions (Schalkwijk et al., 2015; Schemann et al., 2020).

The few observational estimates of mass-fluxes that exist for deep convection, are based on short-term field campaigns. Early on, heat and water budget analyses applied to radiosonde-arrays were combined with some simple assumptions to provide indirect estimates of the bulk-properties of convective mass-fluxes in both deep (e.g., Yanai et al., 1973) and shallow convection (e.g., Nitta, 1975; Nitta & Esbensen, 1974). Direct measurements of vertical velocities in convection became available from aircraft campaigns (e.g., Anderson et al., 2005; Byers & Braham, 1949; LeMone & Zipser, 1980; Marwitz, 1973; May et al., 2008). While providing several breakthroughs in our understanding of tropical convection, the small-scale nature of these observations and the absence of concurrent knowledge of the distribution of clouds over a large area prevents their usage in evaluating the mass-flux concept.

More recently, long-time radar observations from both space and the ground have been used to extensively study the behavior of tropical convection and its relationship to the state of the larger-scale atmosphere. Examples include the Tropical Rainfall Measurement Mission (TRMM, Kummerow et al., 1998) data sets to study convective characteristics, such as convective vigor (Zipser, 2003), types of convective systems (Houze et al., 2015; Nesbitt et al., 2000) and the role of stratiform processes in tropical rainfall (Schumacher & Houze, 2003). Recent studies using a more than a decade long calibrated radar data set acquired at Darwin, Australia (Jackson et al., 2018), specifically retrieved the fractional area covered by convection and related it to precipitation and the large-scale sate of the atmosphere (e.g., Davies et al., 2013; Louf et al., 2019). They found that convective rainfall in the radar domain (≈130 km radius) was very strongly related to the area fraction of active convective cells and that this area fraction was generally small. This important finding indicated that predicting area fraction is an important step in determining precipitation and hence the overall heating in a convecting column.

Long-term measures of vertical velocity are not as trivial to obtain as for area fraction. Nevertheless, they are essential for a better evaluation of the mass-flux approach in GCMs. Some recent studies (e.g., Giangrande et al., 2013, 2016; Kumar et al., 2015) used wind profiler retrievals to attain long-term measurements. A limitation of these studies is the set of assumptions made to use observations at a point location to describe mass-flux at the scale of a GCM grid-box. To overcome this limitation, a later study from Kumar et al. (2016) proposed a parametric equation of vertical velocity inside convective updrafts as a function of radar reflectivity products: the 0-dBZ echo top height (ETH) and the height-weighted reflectivity index $\left(Z_{HWT}\right)$. The present work makes use of this parametric approach to determine mass-flux and, in turn, the rate of mixing between the updrafts and the environment (entrainment/detrainment) (Arakawa et al., 1974).

A recent study from Wang et al. (2021) directly compares the simulated radar reflectivity profiles from a GCM (the Energy Exascale Earth System Model) with ground-based S-band radar measurement, and found that the GCM severely underestimates echo top height. This underestimation of the height of convection results in erroneous mass-fluxes.

Observations on a scale of 100 km from a scanning C-band dual-polarization radar (CPOL; Keenan et al., 1998) in Darwin, are used in this paper. The Darwin region experiences a tropical climate with a dry and a wet season, the latter typically starts in late November or early December and lasts until late April. The wet season brings with it heavy monsoonal downpours and cyclone activity. This, together with the unique topography and the availability of a comprehensive long-term observational record, makes the Darwin region an ideal location to study different regimes of tropical convection (Davies et al., 2013; Kumar et al., 2015, 2016).

The aim of this study is to provide observationally based profiles of convective mass-flux, net fractional entrainment and their constituents using the C-band dual-polarization radar (CPOL; Keenan et al., 1998). With the quantities attained, a second goal is to investigate the relative role of area fraction and vertical velocity in determining the magnitude and shape of mass-flux profiles.

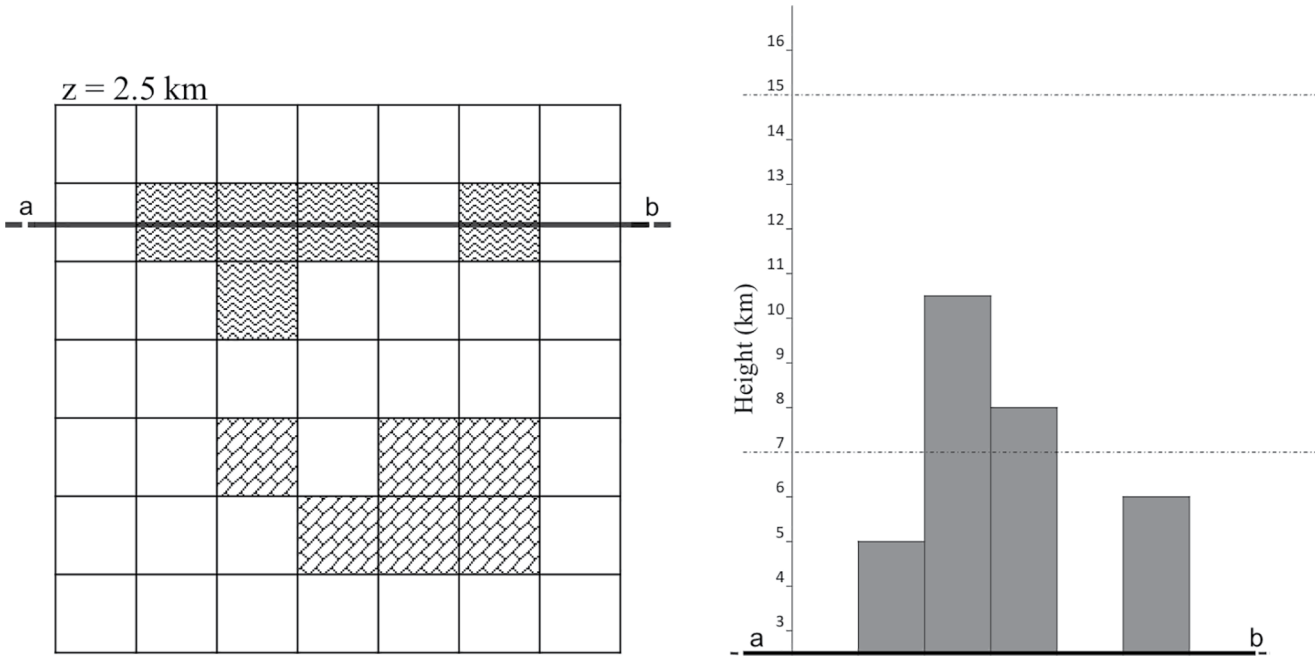

Figure 1. Schematic representation of a scene. The left panel shows three groups of rainy pixels (clouds) classified at $z_b = 2.5$ km: two are convective (wavy patter) and one is classified as stratiform (brick pattern). On the right panel a cross section taken within the convective clouds shows the vertical extent of convective pixels from 2.5 km to the respective 0-dBZ echo top height. The dashed lines mark the 7 and 15 km levels.

The article is organized as follows. In Section 2 the data set used for the study is introduced. Section 3 describes the mass-flux equation and the assumptions used to derive this quantity. Section 4 presents the main results of the analysis for the full data set (Sections 4.1 and 4.2) and for composites of radar scenes with different echo top heights (Section 4.3). Lastly, the findings are discussed and the conclusions are drawn in Section 5.

2. Data

This study uses 13 wet seasons of data gathered by a C-Band Polarimetric radar (CPOL) located near Darwin, Australia (12.25°S, 131.04°E) (Keenan et al., 1998). The measurements cover the period of October 2001 to April 2015, with a gap in 2008, when the radar antenna and receiver needed replacement.

Measurements are available with a time resolution of 10 min, which is the time needed for the radar to perform a full three-dimensional scan. In this work each full radar scan will be referred to as a scene. Only measurements within the range 20–120 km from the radar location are considered. This accounts for both the cone of silence around the radar and minimizes any range-dependence issues far away from the radar (Kumar, Jakob, et al., 2013). The data is interpolated onto a three-dimensional regular grid with a 2.5 × 2.5 km horizontal spacing and 0.25 km vertical spacing (Δz) ranging from 2.5 to 13.5 km above the surface. These vertical limits were used elsewhere (e.g., Kumar, Jakob, et al., 2013) and allow to minimize any issues that might occur during the interpolation of the radar data onto the Cartesian grid.

For each vertical column defined by the grid, the data set includes:

1. *A convective/stratiform classification for each rainy grid point.* Radar pixels are classified at 2.5 km as either convective or stratiform using the algorithm of Steiner et al. (1995). This method takes into account the difference of a pixel's reflectivity with the background intensity to identify convection. All pixels with radar reflectivity larger than 40 dBZ or greater than a fluctuating threshold, depending on the area-averaged background reflectivity, are classified as convective. It also classifies sufficiently intense precipitation next to a convective pixel as convective. Other precipitating radar pixels are classified as stratiform. The left panel of Figure 1 helps visualizing the outcome of this classification in an simplified

gridded domain. The wavy pattern is for convective pixels and the brick pattern is for stratiform pixels. This study makes use of the convective pixel information only.

2. *The 0-dBZ echo top height* (ETH). This is the height where 0 dBZ at the top of a column of consecutive reflectivity values greater than zero is reached. This has been shown to be a reasonable proxy of cloud top height (CTH) as demonstrated by Casey et al. (2012) and Kumar, Jakob, et al. (2013). In particular, Casey et al. (2012) show that for cumulus congestus, the 0-dBZ echo top height is about 1 km lower than satellite based cloud top height (i.e., CloudSat; Stephens et al., 2002). This approximation is about half the error that a model such as CAM5 (Neale et al., 2010) makes in estimating cloud top height, as shown in M. Wang and Zhang (2018). We acknowledge this approximation as a limitation of our study, nevertheless the advantages of using a single instrument (CPOL) frequently scanning an area of the size of a GCM grid-box in full three dimensions far outweigh this small limitation.
   Convective columns, a proxy for convective clouds, are then defined as the vertical region from the lower measurement level at 2.5 km to the 0-dBZ height for each convective pixel. This is visualized in the right panel of Figure 1. Here we note that this definition of convective columns may exclude portions of tilted updrafts. The related implications are discussed in Section 5.
3. *The height-weighted reflectivity index (Z_{HWT})*. Kumar et al. (2016) found that the intensity of convection, expressed through the vertical velocity in convective drafts, is strongly related to a height-weighted sum of the radar reflectivity Z over the the whole column, defined as

$$Z_{HWT} = \log_{10} \sum_k Z \cdot z_k, \tag{1}$$

where z is the height in km. Compared to the logarithm of a simple sum over the column of the reflectivities, Z_{HWT} provides a better link to the vertical velocity throughout the evolution of a convective cell. The height-weighting in Equation 1 gives additional weight to the upper part of updrafts, in which velocities tend to be stronger, while reflectivities tend to be lower due to the presence of ice.

As a key goal of this work is to study vertical profiles of convective mass-flux (see below), only scenes where convection occurs in at least one pixel and covers at least two vertical layers are chosen for analysis. This criterion ensures that the datasets includes scenes with very small convective areas (down to 2.5 × 2.5 km) and well represents the climatological conditions of the Darwin area under precipitating convection. It is worth noting that the CPOL radar only detects precipitation-size particles. As a result, non-precipitating clouds are not included in the analysis and all results relate to precipitating convection only.

3. Estimation of Convective Mass-Flux

The goal of this study is to use the observations described above to estimate bulk mass-flux profiles for every convective scene in the data set. For simplicity, downdrafts are disregarded so that the resulting mass-flux only refers to positive upward vertical velocities inside convection. As the data set provides a very high time resolution of 10 min, sequences of radar scenes will not be independent of each other. As this is a first attempt at exploiting the radar record to study mass-flux characteristics, a simple diagnostic approach is used, that is each scene is treated as independent and information about the life cycle of convective cells is not taken into account. This matches common practice in cumulus parametrizations used in weather and climate models. As mass-fluxes cannot be directly measured, the present study applies the approach proposed by Kumar et al. (2016), in which the mass-flux is computed from observational estimates of area fraction and vertical velocity within each radar scene, as

$$M(z) = \rho(z) w(z) a(z), \tag{2}$$

where $\rho(z)$ is the density, $w(z)$ is the vertical velocity averaged over all convective clouds (see below), and $a(z)$ is the fractional area of the radar scene that is covered by convective clouds. Note that all variables are function of height (z). Since the density ρ does not vary strongly with time we use a climatological time independent profile derived from a variational analysis algorithm (Zhang & Lin, 1997) applied to the ECMWF Interim Reanalysis (Dee et al., 2011) for the Darwin region (Davies et al., 2013; Louf et al., 2019). The estimation of area fraction and vertical velocity is described next.

3.1. Estimation of Area Fraction

The area fraction covered by convective clouds as a function of height is estimated by combining the results of the convective-stratiform classification algorithm with the estimate of cloud top height for each pixel. As discussed above, reflectivity at the lowest level (2.5 km height) for each radar scene is used to classify each pixel as either convective or stratiform using the algorithm by Steiner et al. (1995). Dividing the area of convective pixels by the total radar scene area provides the convective area fraction at the 2.5 km-level.

Next, the 0-dBZ cloud top estimate for all convective pixels is used to determine the cloud depth at each individual convective pixel. It is worth noting that cloud depth can vary strongly from pixel to pixel. From the cloud top information it is then straightforward to calculate the number of pixels that are convective at each height level above the 2.5 km-level and from that the convective area fraction as a function of height, $a(z)$. As the cloud top algorithm requires consecutive layers of reflectivity above the 0-dBZ threshold for a layer to be classified as cloud, the fractional area can only stay constant or decrease with height. Once more, it is important to remember that the area fraction refers only to grid cells where precipitating convection occurs and that grid cells with stratiform clouds do not contribute to the cloud fraction.

Much of the significant convection in our domain, that is events with a relatively large area fraction, occur in the low-level wind shear environments of the active Australian monsoon or during monsoon breaks, where they are dominated by diurnally forced convection associated with the complex topography (Kumar, Protat, et al., 2013).

3.2. Estimation of Updraft Vertical Velocity

To estimate the updraft vertical velocity a statistical model is applied that relates velocity to cloud depth and reflectivity, as proposed by Kumar et al. (2015) and Kumar et al. (2016). The model was developed using retrievals of in-cloud vertical motion from dual frequency wind profiler observations within the CPOL radar domain (Williams, 2012). The main equations of the statistical model as it is applied here are presented below. For a detailed description, parameter estimation and evaluation of the statistical model the reader is referred to Kumar et al. (2016). We further discuss this method for vertical velocity retrieval in Section 5 as it is not the only one available in literature, though it is best suited for the Darwin region.

The model starts by using the 0-dBZ echo top height to classify convective pixels into three cumulus modes. It then assigns an initial idealized updraft wind profile shape (see Equation 3) to each radar pixel depending on its 0-dBZ echo top height.

The initial idealized shape of the updraft wind profiles for the three cumulus modes are defined as

$$w_u(z) = \begin{cases} 0.404z + 0.9922, & \text{for ETH} \le 7\,km \\ -0.0016z^4 + 0.0519z^3 - 0.571z^2 + 2.7z - 2.7351, & \text{for } 7 < \text{ETH} \le 15\,km \\ -0.0454z^2 + 1.0889z - 0.8963, & \text{for ETH} > 15\,km \end{cases} \quad (3)$$

where the subscript u is used to distinguish the quantity from the vertical velocity w defined in Equation 4. Having determined the initial shape of the vertical velocity profile as a function of echo top height at a single pixel, the shape is adjusted and the magnitude is estimated. This is achieved by scaling the profiles from Equation 3 with a reflectivity-dependent scaling factor such that the vertical velocity at each convective pixel, i, is given by:

$$w_i(z) = w_u(z)T_Z(z), \quad (4)$$

where w_i is in m/s and T_Z is a dimensionless scaling factor. T_Z is expressed as

$$T_z(z) = \left(\frac{w_{res} + \overline{w}_u}{\overline{w}_u}\right)\left(\frac{w_u(z)^{0.5}}{\overline{w}_u^{0.5}}\right), \quad (5)$$

where $\overline{w}_u$ is the column-mean updraft velocity estimated from Equation 3. $\overline{w}_u$ reads

$$\overline{w}_u = \frac{\sum_k w_{u,k} \cdot \Delta z}{\text{ETH} - z_b}, \quad (6)$$

where the summation is over all discrete levels, spaced $\Delta z = 0.25$ km, from $z_b = 2.5$ km to ETH.

Importantly, a reflectivity-dependent velocity, w_{res} is introduced as

$$w_{\mathrm{res}} = a + bZ_{\mathrm{HWT}}, \tag{7}$$

where a and b are empirical coefficients in m/s and their formulation was suggested by Kumar et al. (2016) as $a = 4.3911 - 1.2381 \cdot \mathrm{ETH}$ and $b = -0.06064 + 0.02095 \cdot \mathrm{ETH}$, where ETH is expressed in km.

w_{res} quantifies the intuitive assumption that the vertical motion at convective pixels with larger reflectivity (note that a height-weighted integral of reflectivity is used) is likely stronger leading to more intense rainfall.

3.3. Estimation of the Bulk Mass-Flux

Once a vertical velocity profile for each convective grid cell has been obtained using the method above, the bulk vertical velocity is calculated by averaging over all convective pixels at each height z to yield

$$w(z) = \frac{\sum_i w_i(z)}{N_{\mathrm{c}}(z)}, \tag{8}$$

where N_{c} is the number of convective pixels at height z.

Combining the result of Equation 8 with the estimate of area fraction discussed in Section 3.1 then allows the calculation of the bulk mass-flux, M, at every level using Equation 2.

4. Results

4.1. Mass-Flux and Its Components

Combining the estimates of area fraction and bulk vertical motion described in Section 3 allows for the calculation of the bulk convective mass-flux for every 10-min radar scene that contains convective pixels. Figure 2 shows the distribution of all components of the mass-flux as from Equation 2. Panel (a) depicts the distribution of mass-flux M, (b) of the convective area fraction a, (c) of the bulk vertical velocity w, and (d) of the product of density and vertical velocity $\rho \cdot w$. In each panel, the solid line depicts the mean value, the dashed line show the median and the dotted lines are the 25 and 75 percentiles of the total mass-flux distribution. All percentiles are calculated separately for each vertical level. We also introduce an index to order the scenes in time and note that the mean profiles are related by the following set of equations:

$$\begin{aligned} \langle w \rangle &= \frac{\sum_{t=1}^{T} w_t a_t}{\sum_{t=1}^{T} a_t}, \\ \langle a \rangle &= \frac{1}{T} \sum_{t=1}^{T} a_t, \\ \langle M \rangle &= \rho \langle w \rangle \langle a \rangle \end{aligned} \tag{9}$$

where the chevrons refer to the temporal average of a quantity and T is the total number of scenes.

The bulk mass-flux profiles (Figure 2a) show a well-known shape, with an increase in mass-flux at low levels, a peak at about 4–5 km above the surface followed by a steady decrease above that level (Betts, 1975; Schiro et al., 2018). The peak mean value of mass-flux is about 0.017 kg/(m^{2}s). The distribution shows a pronounced skewness at all levels, with the median values being much smaller than the mean. The peak median value is 0.017 kg/(m^{2}s) and it occurs slightly lower in the atmosphere than the peak mean value. The profile associated with the lower quartile indicates the prevalence of convective clouds with tops below 8 km and very weak mass-fluxes. The upper quartile shows a peak value near 0.017 kg/(m^{2}s) with a more rapid decrease of mass-flux above the peak level than the mean or median. The pronounced skewness of the distribution suggests that, for the large majority of the radar scenes, mass-flux is small. The few occasions with very strong mass-fluxes skew the mean toward larger values. In fact, the largest mass-fluxes in Figure 3 correspond to a case of a tropical cyclone approaching Darwin in 2003 leading to wide-spread convection.

Decomposing the bulk mass-flux into contributions from the convective area fraction (Figure 2b) and bulk velocity (Figure 2c) provides a first insight into how the mass-flux profiles attain their distinct shape. First, it is evident that the skewness of the bulk mass-flux distribution is a result of a skewed distribution of convective area fraction, while for the vertical velocity median and mean values are almost identical.

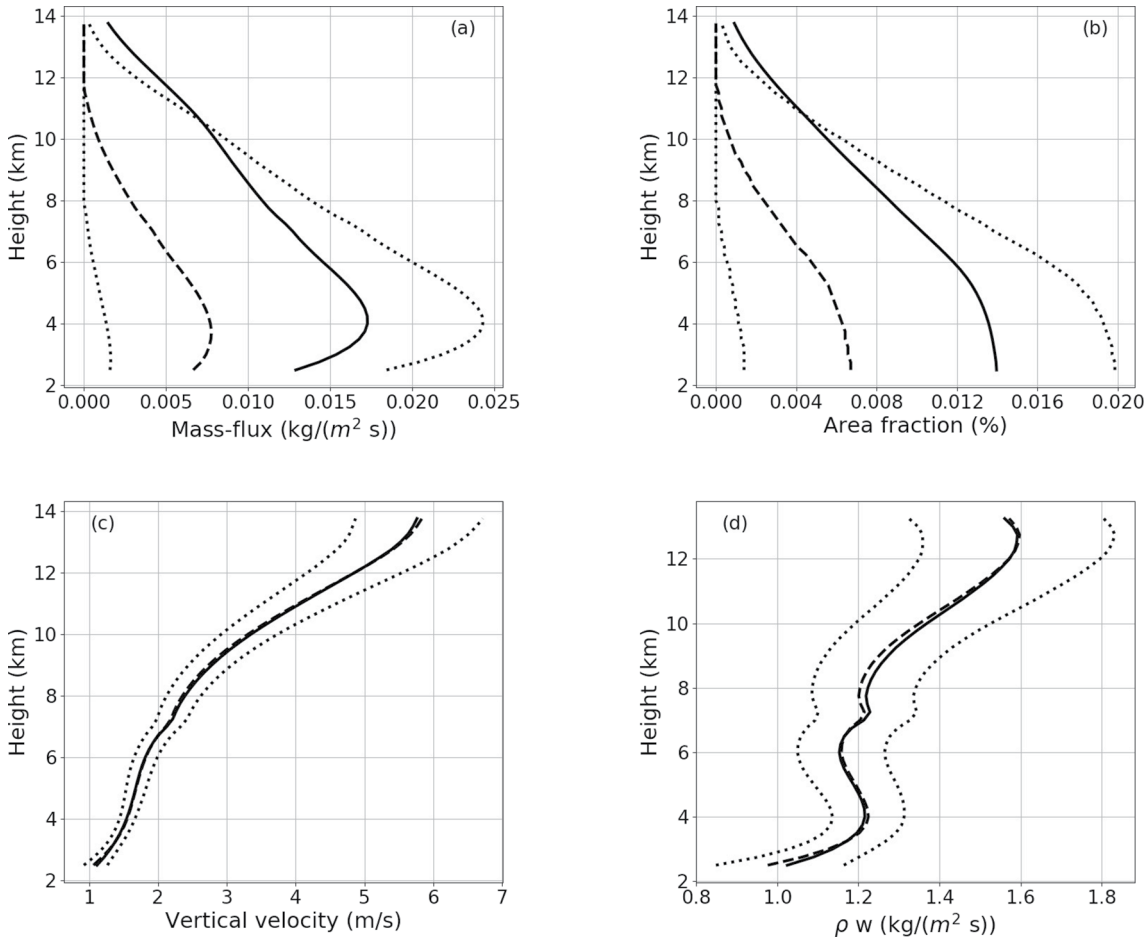

Figure 2. Temporal mean (solid), median (dashed), lower and upper quartiles (dotted) of (a) bulk mass-flux, (b) convective area fraction, (c) bulk vertical velocity, and (d) the product of density and bulk vertical velocity for the entire data set.

It is worth remembering that, a decrease in area fraction indicates a loss of convective pixels with weak in-cloud vertical motion or low condensate mixing ratio. Therefore, the increase of the bulk-vertical velocity with height is not only a result of in-cloud buoyancy but also a result of fewer but stronger updraft that constitute the ensemble mean.

The increase in mass-flux below 4 km is associated with an increase in bulk vertical velocity. The convective area fraction is almost constant below 4 km, leading the in-cloud mass-flux ($\rho \cdot w$) to dominate the shape of the area average mass-flux. Between 4 and 6 km, the bulk vertical velocity does not increase significantly and the reduction of fractional area is more pronounced compared to lower levels. As a result, the mass-flux decreases with height in this 2 km layer. Above 6 km, both vertical velocity and in-cloud mass-flux are increasing with height. Nevertheless, a rapid decrease of bulk mass-flux is observed as a result of a rapid decrease in convective area fraction. This important characteristic of the observed cloud ensemble is a direct result of fewer and fewer clouds reaching the upper levels of the atmosphere. The small discontinuity at 7 km is a direct result of the vertical velocity model for different cloud depth (see Equation 3) not matching between cloud types at this level.

Given the large skewness of the bulk mass-flux distributions it is worth investigating its behavior near the upper tail of the distribution. For this purpose Figure 3 shows the mean (solid line) and the 90th, 95th and 99th percentiles (dotted lines) of the bulk mass-flux, convective area fraction and bulk vertical velocity. The figure also shows four individual profiles chosen as having the maximum mass-flux of all scenes at 2.5 km (blue), 5 km (red), 10 km (green), and 13.5 km (orange). The figure strongly supports the notion that it is the convective area fraction that largely determines the magnitude of the bulk mass-flux. For example, the

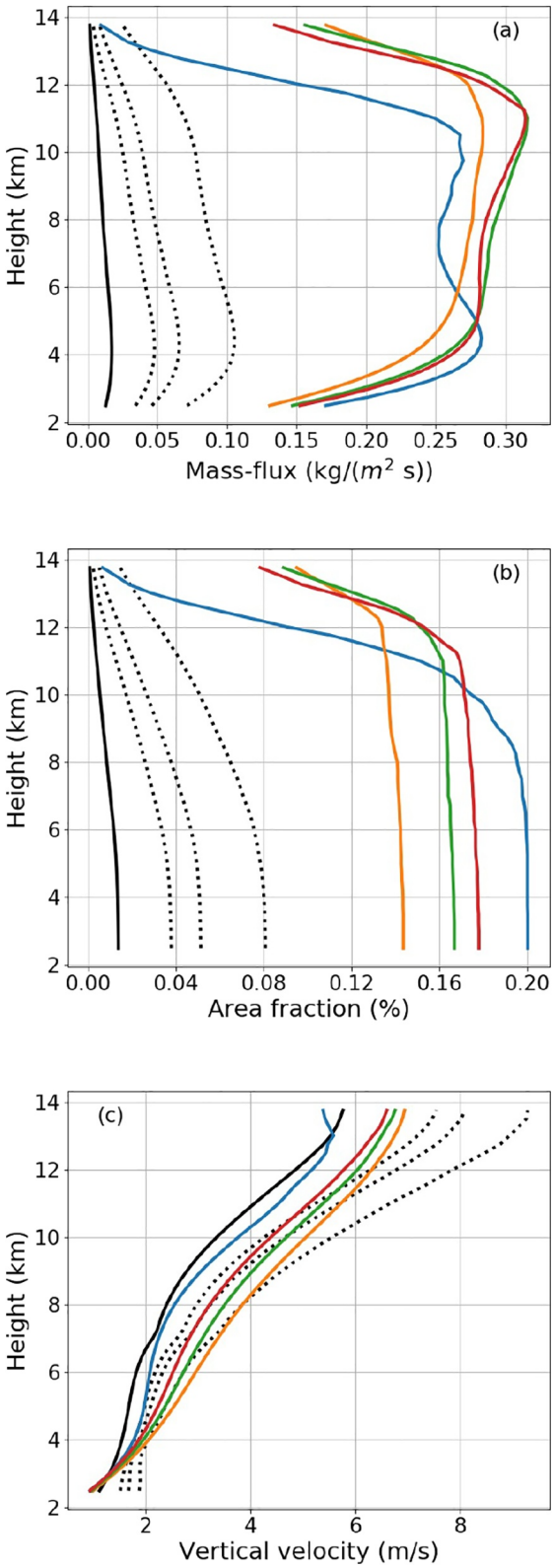

Figure 3. Temporal mean (black solid), 90th, 95th, 99th percentiles (black dotted) and the strongest mass-fluxes at various heights (see text). The three panels show bulk (a) mass-flux, (b) area fraction, and (c) vertical velocity.

scene with the strongest mass-flux at 2.5 km (blue line) also shows an exceptionally large area fraction at this level but its value of vertical velocity is not particularly strong.

There is also a noteworthy difference between the shape of the strongest bulk mass-flux profiles and those of the mean or median. Whereas the mean profile decreases with height, the strongest individual mass-flux profiles remain constant or even increase slightly with height. Figure 3 reveals that this is the result of an almost constant convective area fraction to a great depth in the atmosphere. The fact that this is not visible in the 95th or even 99th percentile of the distribution does indicate that this bulk mass-flux behavior is very rare. Given the strong connection of bulk mass-flux to area average rainfall (Louf et al., 2019) these events are likely the most extreme rainfall events in the region (in an area average sense) and their difference in mass-flux behavior warrants further study in the future.

4.2. Vertical Derivatives

To gain more insight into the vertical structure of the bulk mass-flux, the fractional change of the mass-flux with height can be related to the fractional change in area fraction and vertical velocity, using Equation 2 as

$$\frac{1}{M}\frac{\partial M}{\partial z} = \frac{1}{a}\frac{\partial a}{\partial z} + \frac{1}{\rho w}\frac{\partial(\rho w)}{\partial z}. \tag{10}$$

In mass-flux models, the fractional change of mass-flux has been related to the fractional entrainment and detrainment rates, ϵ and δ, as (Tiedtke, 1989):

$$\frac{1}{M}\frac{\partial M}{\partial z} = \epsilon - \delta. \tag{11}$$

The fractional entrainment ϵ describes the inflow of environmental air into the cloudy updraft, while the fractional detrainment δ describes the outflow of cloudy air into the environment. Although the two terms on the right hand side of Equation 10 do not coincide respectively with ϵ and δ, the definition of convective column adopted here implies that the fractional change in area fraction only contributes to the detrainment. Differently, the fractional change in vertical velocity can be positive or negative, thus contributing to the fractional entrainment or to the fractional detrainment.

Whereas there have been numerous studies that determined fractional entrainment and detrainment rates from numerical simulations (e.g., Carpenter et al., 1998; Lin & Arakawa, 1997; Romps, 2010; Siebesma et al., 1996), direct observations of entrainment and detrainment are close to impossible, even for storm-penetrating aircraft. In literature, there have been few indirect estimates of entrainment and detrainment profiles from satellite measurements (e.g., Masunaga & Luo, 2016). Here, Equation 10 is applied to ground-based radar measurements to provide a first climatological estimate of the net effect of entrainment and detrainment.

Using the data of the mass-flux, the area fraction and the vertical velocity, all three terms in Equation 10 can be determined and their temporal averages are displayed in Figure 4. There are several distinct regions in the profile of the vertical derivative of the mass-flux (Figure 4a). Below roughly 4 km, the derivatives are positive. This is the result of a strongly

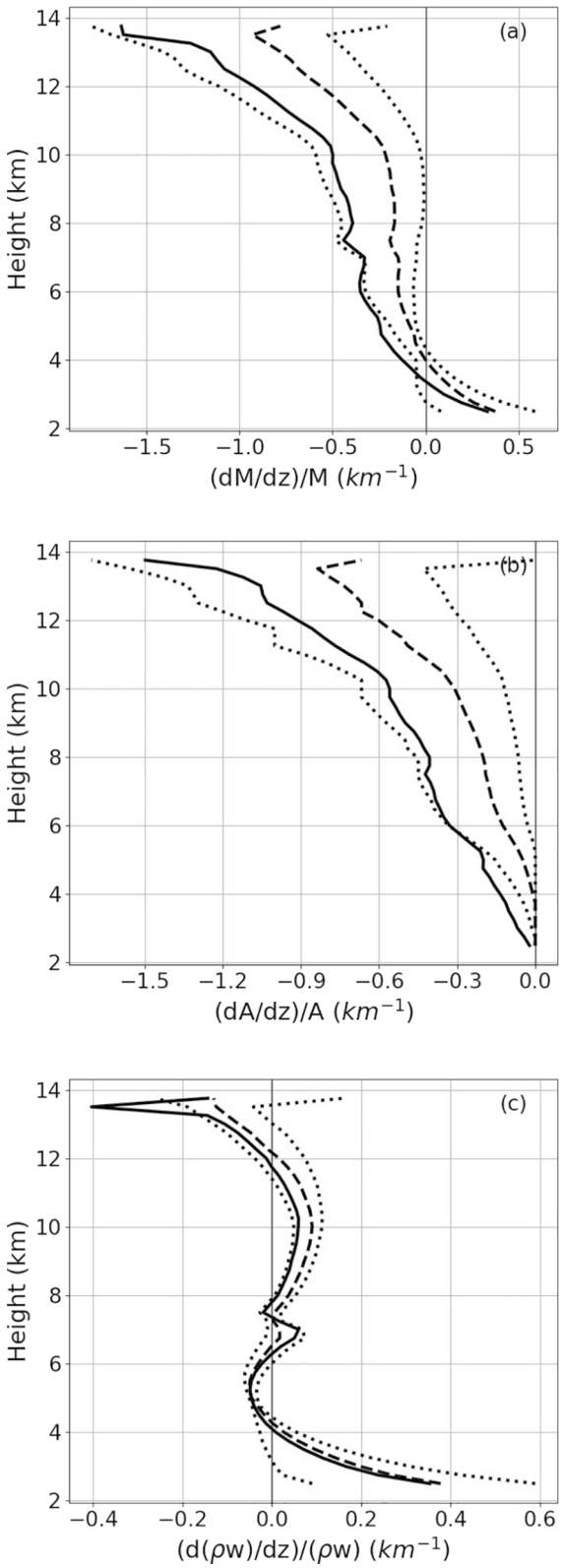

Figure 4. Temporal mean (solid), median (dashed), and upper and lower quartile (dotted) of the normalized vertical derivative of (a) mass-flux, (b) area fraction, and (c) the product of density and vertical velocity as a function of height.

positive vertical derivative of the vertical velocity term (Figure 4c), while the median of the vertical derivative of area fraction is zero in this region (Figure 4b). Above 4 km, the vertical derivative of the mass-flux is negative. The derivative is fairly constant between 5 and 10 km and then increases in magnitude. This is is the result of a steadily strengthening negative vertical gradient in normalized area fraction, while the bulk vertical velocity gradients are small. We note once again that the spike observed at 7 km in Figure 4c is an artifact of the switching of calculation of the updraft vertical velocity for clouds deeper than 7 km from that for shallower ones (Equation 3). While this limits our interpretation of the vertical velocity evolution itself, the presence of a relatively smaller spike in the mass-flux derivative in Figure 4a corroborates the hypothesis that the results for the overall mass-flux evolution are dominated by the much more directly observed convective area fraction.

As discussed above, the fractional change of mass-flux represents the net effect of entrainment and detrainment on the bulk mass-flux (e.g., de Rooy et al., 2012; Siebesma, 1996; Tiedtke, 1989). When positive, there is net gain of mass in cloudy air through entrainment from the environment, while negative values indicate a net transfer of cloudy mass to the environment through detrainment. Our results show that, on average, convective cloud ensembles in the study area experience a strong and steady net entrainment from their base to about 4 km, moderate net detrainment between 4 and 10 km and strong net detrainment above 10 km. We note that this behavior represents the entire cloud ensemble and is likely a combination of different behaviors of clouds of varying depth. To investigate this further, the next section will divide the data set into scenes that are characterized by clouds of different depth to investigate how the presence of different "cloud modes" might shape the overall mass-flux profile in Figure 2.

4.3. Composite Analysis by Maximum Echo Top Height

We take advantage of the echo top height (ETH) information in our data set to divide the radar scenes based on the maximum echo top height (ETH_{max}) found in each of them. Following the study of Kumar, Jakob, et al. (2013) we choose the threshold values of 7 and 15 km to define three classes of scenes: $ETH_{max} \leq 7$ km, $7\text{ km} < ETH_{max} \leq 15$ km, and $ETH_{max} > 15$ km. We then analyze the composite mass-flux behavior for each of these three classes to see how they may shape the overall mass-flux profiles discussed above. We adopt the terminology of Kumar, Jakob, et al. (2013) and refer to these scenes as congestus, deep and overshooting. We use this nomenclature in a loose sense and note that unlike in Kumar, Jakob, et al. (2013), who classified individual clouds in this way, we assign the name to an entire scene if the maximum height reached by any cloud in the scene fulfills the criterion that defines the class.

Figure 5 shows the ETH distributions for all convective pixels for the entire data set (Figure 5a) and for three sub-groups of scenes selected based on the maximum ETH found in them (Figures 5b–5d). The overall ETH distribution (Figure 5a) is quite broad with ETH between 6 and 12 km almost equally likely. There are small peaks at 7 and 9 km, respectively. Selecting scenes where the maximum ETH in the scene is below 7 km by definition eliminates all pixels with higher ETH. 21% of the scenes in our data set fall into this category. They represent relatively shallow

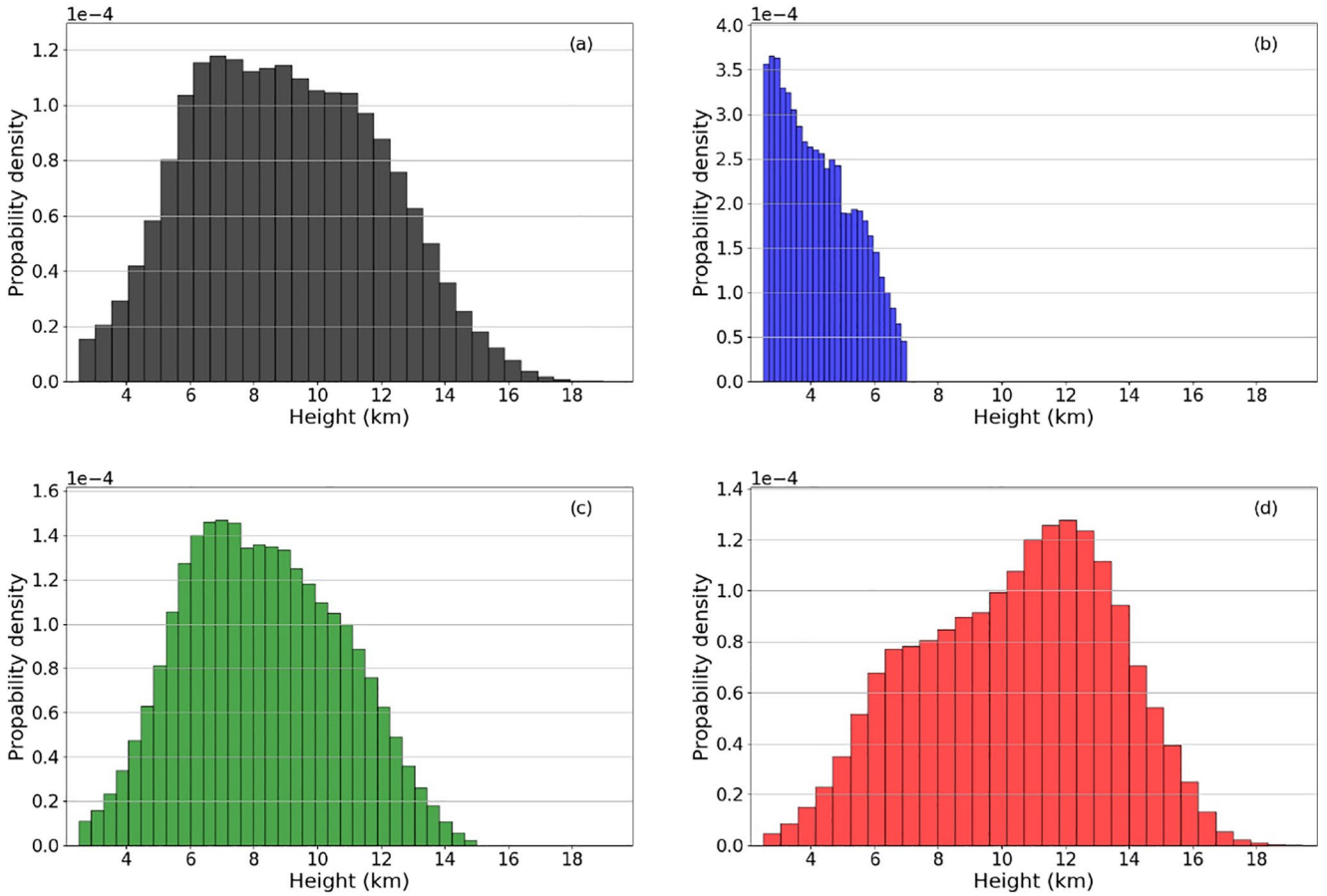

Figure 5. Frequency distribution of 0-dBZ ETH, used as a proxy for the height of convection in a pixel. In (a) all scenes of the data set are used, (b) refers to scenes where the tallest convective cell is lower than 7 km: Composite 1, (c) is obtained using scenes with the maximum extent of convection between 7 and 15 km: Composite 2, (d) is obtained from scenes with convective cells rising taller than 15 km: Composite 3.

congestus cloud fields. We note that these clouds still contain sufficient precipitation to be detected by the radar and should not be confused with non-precipitating shallow cumulus clouds, which are not detectable by the radar. The ETH distribution for the congestus class shows a rapid decrease of cloud top likelihood from the minimum detectable value (2.5 km) to the maximum (7 km) (Figure 5b). This is consistent with a strong reduction of cloud area with height that is frequently reported in shallow cumulus fields (Brown et al., 2002; Siebesma et al., 2003; VanZanten et al., 2011), which according to our results translates to congestus cloud fields as well.

The shape of the distribution of deep convective cloud fields is very similar to the overall distribution except for the drop-off in likelihood which occurs at lower ETH and the lack of clouds deeper that 15 km, which has been introduced by the definition of deep convective scenes (Figure 5c). This similarity is in large part due to the fact that 63% of all scenes fall into this category. Remarkably, while by definition the maximum ETH in the scene is above 7 km, the distribution still peaks at 7 km. This indicates that even in cloud fields that contain deep convection, the most frequently observed clouds in the scene have moderate ETH between 6 and 8 km.

Scenes that contain overshooting convection constitute 16% of the total data set. The ETH distribution in the presence of overshooting clouds is distinctly different from all other categories (Figure 5d). The maximum likelihood of ETH shifts upward to values between 12 and 13 km, indicating the presences of a relatively large number of deep clouds (Figure 3). These scenes therefore represent the most wide-spread vigorous deep convection found in our data set.

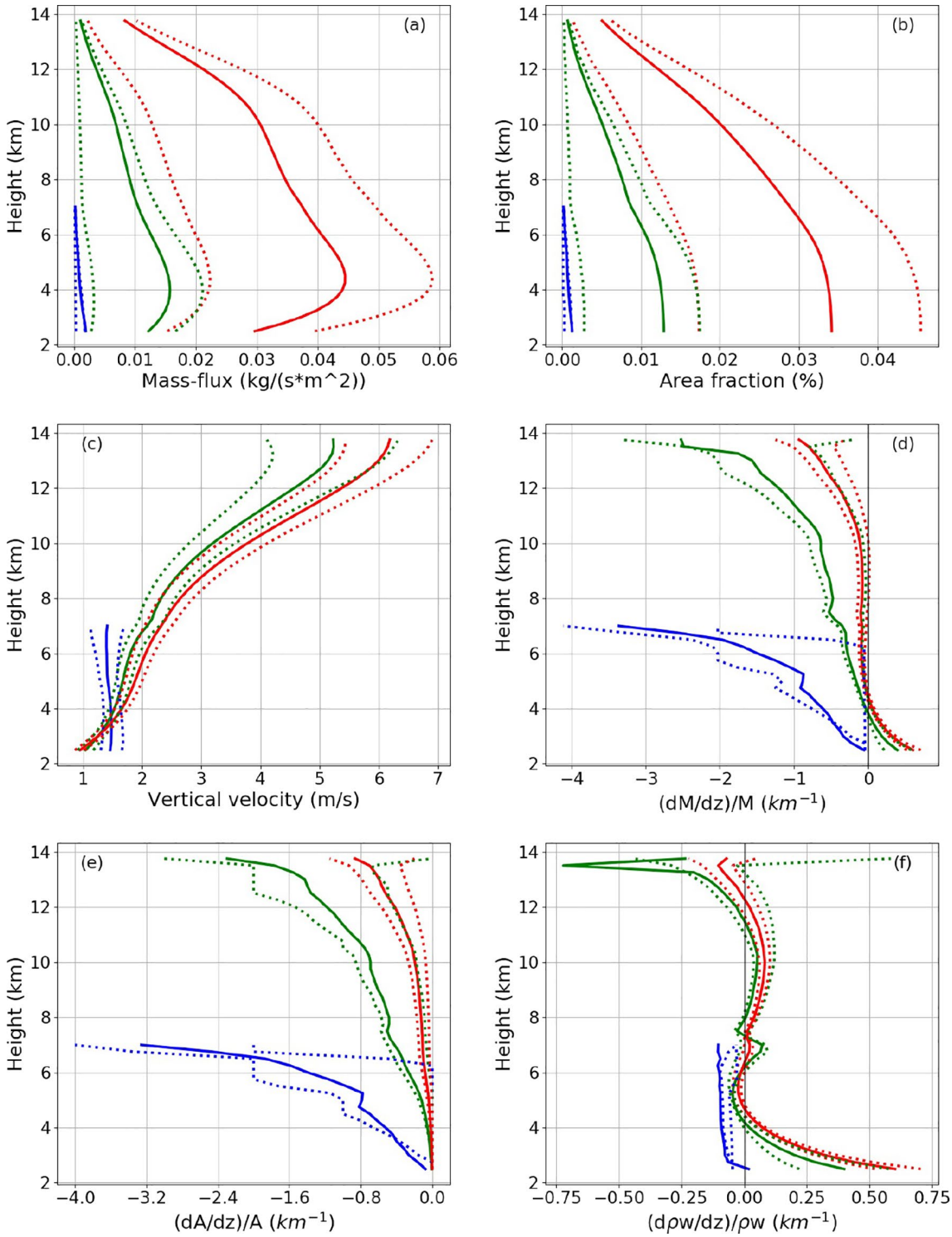

Figure 6. Vertical profiles of (a) bulk mass-flux, (b) area fraction, and (c) vertical velocity as well as their normalized vertical derivatives (d–f) for the congestus (blue), deep (green) and overshooting (red) classes of radar scenes. Solid lines indicate the median and dashed lines the 25th and 75th percentile, respectively.

Having separated all radar scenes into maximum ETH categories, we now analyze the vertical structure of the mass-flux, its components and their vertical derivatives (Figure 6). Each class of radar scenes is represented by the same colors used in Figure 5. There is a very clear separation in mass-flux strength between the categories (Figure 6a). The congestus class is characterized by very small mass-fluxes while scenes with

overshooting convection show very large mass-fluxes. The deep class shows moderate values of mass-flux. It is evident that the main difference between classes comes from the convective area fraction (Figure 6b), while the updraft velocities (Figure 6c) are of similar order of magnitude in all classes, with the overshooting class showing values roughly 1 m/s larger than those for the deep class.

There are notable differences in the vertical structure of mass-flux between the three classes. In congestus convection, the maximum mass-flux is found at the lowest level in the data set (2.5 km) and is decreasing with height at all levels above with an entrainment rate that increases with height (Figure 6d). Once again, this behavior is largely the result of a rapid decrease of area fraction with height (Figure 6e) accompanied by a weakly decreasing velocity component (Figure 6f). For both deep and overshooting convection, the mass-flux increases with height below 4 km with a larger rate found in overshooting convection. This larger rate of mass-flux increase at low levels is the result of larger rates of increase in the vertical velocity component, while the vertical derivatives of area fraction are close to zero for both deep and overshooting cases. Above 4 km the vertical derivative of mass-flux is negative for both deep and overshooting convection mostly owing to negative derivatives for area fraction. Notably, the values for deep convection are several times larger than those for overshooting convection, indicating a more rapid decrease of mass-flux in the middle to upper troposphere. The apparent acceleration of the updrafts between 8 and 12 km is also slightly larger in the overshooting case. We note again that this "acceleration" in the bulk velocity is likely the result of the loss of weaker clouds from the ensemble and does not necessarily indicate an increase of velocity in individual clouds.

5. Discussion and Conclusions

The aim of this study was to derive convective mass-fluxes and their constituents on the scale of a GCM grid-box from a C-band polarimetric radar and thereafter investigate the relative role of area fraction and vertical velocity in determining mass-flux. We made use of observational estimates of mass-flux spanning 13 wet seasons in the tropical region of Darwin. To the authors' knowledge, this is the first time that such longstanding measurements are exploited to retrieve a climatology of mass-flux. The exceptionally comprehensive data set allowed to elucidate on the statistical distribution of these profiles.

The analysis showed that, in this area, the ensemble mass-flux of precipitating convective clouds peaks at 4 km. Its distribution is positively skewed with the tail highlighting the presence of rare but very strong mass-fluxes. It was also found that the skewed distribution and the magnitude of mass-flux are largely determined by the fractional area covered by convection, while the in-cloud vertical velocity plays a less significant role. The magnitude of mass-flux found in our study is similar to what shown by Schiro et al. (2018) for the central region of the tropical Amazon basin. Compared to other studies which also estimate precipitating convective area fraction from scanning radars in the tropics (e.g., Giangrande et al., 2016; Kumar et al., 2015), the magnitude of area fraction, and consequently of mass-flux, shown in Figure 2 appear almost an order of magnitude smaller. This mirrors the definition of convective scene adopted in this study. Kumar et al. (2015) used averages over 3-hourly windows and discarded all windows with no presence of convective clouds. Similarly, for the Amazon basin, Giangrande et al. (2016) considered 1, 3, and 6-hr intervals that featured a minimum 1% convective area fraction. Another recent study from Jeyaratnam et al. (2021), and based on satellite measurements, showed similar large magnitudes of area fraction as a result of the same 3-hr averaging method. Their choice reflects conditions on longer time scales compared to our 10 min scale. The different methods for temporal averaging do not affect the shape of the profiles but only their magnitude, larger values of area fraction would strengthen even more the dependency of mass-flux to the areal component observed in our analysis.

Although the mass-flux profiles shown in this study are relatively similar to the one shown by Schiro et al. (2018), we argue that their interpretation of the results can be misleading with respect to the relative role of area fraction and vertical velocity in determining the mass-flux profile. Other than the convection criterion used here and based on Steiner et al. (1995), Schiro et al. (2018) limit their data set to updrafts which extend to >9 km and with vertical velocities >1 m/s in at least 10% of the profile. This choice results in constant profiles of area fraction up to 9 km, thus strongly influencing the results obtained when analyzing the vertical derivatives of mass-flux and its components. The dominant role of convective area fraction

in determining mass-flux was suggested in several other studies (e.g., Jeyaratnam et al., 2021; Kumar et al., 2015; Masunaga & Luo, 2016) including LES experiments (e.g., Böing et al., 2012; de Rooy & Siebesma, 2010) and it is confirmed in our study. These results encourage parameterization methods that aim to estimate area fraction and vertical velocity separately (de Rooy & Siebesma, 2010; Peters et al., 2013, 2017; Siebesma et al., 2020).

It is important to remember that the results presented above can be affected by the definition adopted for convective column. In fact, we perform a convective-stratiform classification only at 2.5 km, thus disregarding the portions of tilted convective systems which are not directly above another convective pixel. There are two important factors that mitigate against this potential shortcoming affecting our conclusions in a major way.

First, as noted in Section 3.1, much of the significant convection in our domain, that is events with a relatively large area fraction, occur in the low wind shear environments of the active Australian monsoon or during monsoon breaks (Kumar, Protat, et al., 2013). The strongest low-level (0–3 km) and mid-level vertical wind shear occurs during the trade wind regime and is limited to about 11% of the scenes, typically in October and November. This regime has the lowest rate of convective activity, consistently with dry continental air masses being advected into the Darwin region.

Second, the relatively coarse resolution of 2.5 km and the interpolation method used to create the Cartesian grid (Jackson et al., 2018) implicitly mitigate against the problem of tilting. If we assume a point centered in our 2.5 km box, the tilt would have to be more than 10° for the cloud top to move to a neighboring pixel at 10 km height and it would have to be more than 25° to move it to a neighboring pixel at 5 km height. Given the low-shear environment in the tropics, we are confident that tilts of this magnitude do not majorly affect our conclusions.

The retrieval of vertical velocity and area fraction in this study is based on simple, nonetheless effective methods which have been largely used in literature. Kumar et al. (2016) compared vertical velocity estimates from radar reflectivity with observations from wind profilers and dual-Doppler radar retrievals. Their analysis showed that the parameterization reproduces the PDF of vertical velocity quite well with a slight underestimation of large values above the 75th percentile. The agreement between velocity profiles is largest below 5 km and decreases with height, this could be due to the error introduced using the 0-dBZ as a proxy for CTH. Care must also be taken in interpreting the results of this study beyond the tropical region of Darwin since this parameterization is specifically calibrated for the Darwin region. Nevertheless, the method has been evaluated against independent datasets and on multiple wet seasons. The reader is referred to Figure 11 in Kumar et al. (2016) where estimates of vertical velocity from radar reflectivity are compared with direct measurements from wind profilers. We also note that the uncertainties of the simple velocity estimation method are further reduced through our use of the bulk vertical velocity, that is the average velocity over all clouds in the scene, thus reducing random errors.

Other approaches to estimate in-cloud vertical velocity have been proposed in recent years, for example Masunaga and Luo (2016) made use of ambient sounding, plume model, and satellite cloud observations. Their approach is limited by the characteristics of the satellite (CloudSat). Although it allows for a better estimate of the CTH, its temporal resolutions and the 2-dimensional nature of the scans do not allow to have a comprehensive sample of convection in a region. We believe that despite the limitations of our study, our data set best serves the purpose of observing mass-flux in an area comparable to a GCM grid-box. Another limitation of Masunaga and Luo (2016) is that the use of the plume model requires observational constraints of turbulent entrainment rates, which are themselves a target of our analysis here.

Figure 7 summarizes the results of this study showing together the mean of the vertical fractional rate of change of mass-flux (solid), area fraction (dash-dot) and in-cloud mass-flux (dash). The reader is reminded of Equation 10 which implies that the solid line in Figure 7 results from combining the dashed line with the dash-dotted line. Each panel includes profiles from all scenes (black) and one of the three classes of scenes defined in Section 4.3: congestus (blue), deep (green), overshooting (red).

All panels prove that the vertical fractional rate of change of mass-flux (solid) mimics the vertical rate of change of convective area fraction (dash-dot), except for the layer below 4 km in scenes with deep or

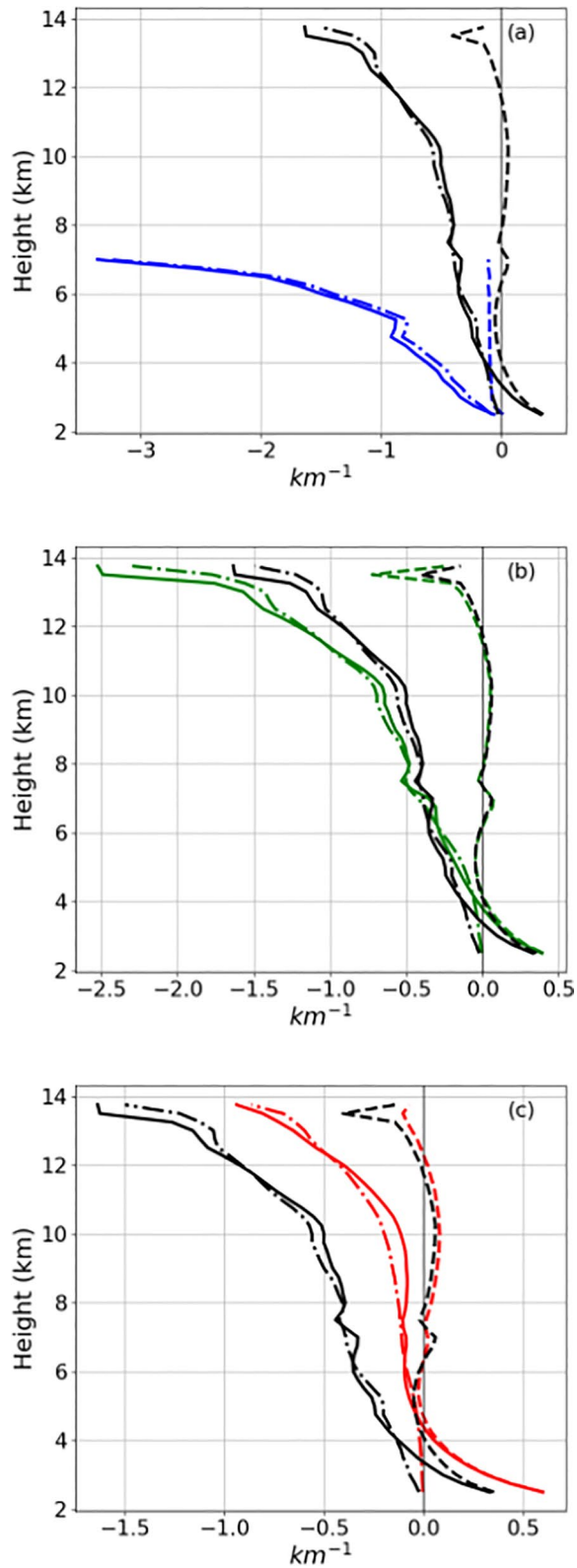

Figure 7. For each composite (Composite 1 [a], Composite 2 [b], Composite 3 [c]), mean profiles of all terms in Equation 10 compared with means attained using all scenes (black lines). Solid line refers to $\frac{1}{M}\frac{\partial M}{\partial z}$, dash-dot line refers to $\frac{1}{A}\frac{\partial A}{\partial z}$, dashed line refers to $\frac{1}{\rho w}\frac{\partial \rho w}{\partial z}$.

overshooting clouds. By separating the data set into composites according to the tallest convective cell, it was possible to demonstrate that the most common cloud field (63% of the scenes) presents the maximum 0-dBz ETH between 7 and 15 km. Remarkably, even in such cloud fields, containing deep convection, the most frequently observed clouds have moderate ETH between 6 and 8 km.

An analysis of the normalized vertical derivative of mass-flux further allowed to elucidate on the mixing process of clouds with the environment (i.e., net entrainment or net detrainment). In fact, positive values in Figure 7 indicate net fractional entrainment while negative values correspond to net fractional detrainment. From the considered ensembles of precipitating convective clouds it is possible to distinguish two regions in the vertical dimension: the first, below 4 km, is dominated by net fractional entrainment; the second, above 4 km, is dominated by net fractional detrainment. The region above 4 km is further divided into two layers. From 4 to 10 km an intermediate reduction rate of mass-flux is observed, while above 10 km mass-flux reduces more rapidly.

As this is a first attempt at characterizing mass-flux from radar reflectivities, we adopted a simple bulk approach where all convective cells in the field are lumped together and the profiles of the ensemble are studied. Although this approach does not provide information on single clouds and their individual mass-flux profiles, the bulk approach was chosen because it is widely used in current GCMs. Furthermore, the methods of this work do not exclude the possibility of performing a similar analysis with a spectral approach. In fact, CPOL radar data are spatially distributed and individual clouds can be identified within a scene (Kumar, Jakob, et al., 2013; Louf et al., 2019).

Despite the great potential of deriving mass-flux from radar reflectivity, this study is based on a single radar location and further investigation is needed before extending our conclusions to other regions of the Earth. Future works should also focus on accounting for the effect of non-precipitating convection as this can sensibly alter the total mass-flux of a cloud field, especially in what we called congestus scenes. This study is a first step in understanding the distribution of ensemble mass-flux profiles in an area comparable to a GCM grid-box. We encourage studies to further exploit the CPOL data set, for example by investigating the temporal evolution of mass-flux profiles or directly compare GCM outputs with these observations.

Data Availability Statement

The radar data set used in this study was provided by Valentin Louf and it is available at the following URL: http://dx.doi.org/10.25914/5f4c857de1bb7.

Acknowledgments
The authors would like to acknowledge the contribution of Louise Nuijens. Christian Jakob acknowledges funding from the Australian Research Council's Centre of Excellence for Climate Extremes (CE170100023).

References

Anderson, N. F., Grainger, C. A., & Stith, J. L. (2005). Characteristics of strong updrafts in precipitation systems over the central tropical Pacific Ocean and in the Amazon. *Journal of Applied Meteorology*, *44*(5), 731–738. https://doi.org/10.1175/JAM2231.1

Arakawa, A. (2004). The cumulus parameterization problem: Past, present, and future. *Journal of Climate*, *17*(13), 2493–2525. https://doi.org/10.1175/1520-0442(2004)017<2493:ratcpp>2.0.co;2

Arakawa, A., Schubert, W. H., Arakawa, A., & Schubert, W. H. (1974). Interaction of a cumulus cloud ensemble with the large-scale environment, Part I. *Journal of the Atmospheric Sciences*, *31*(3), 674–701. https://doi.org/10.1175/1520-0469(1974)031<0674:ioacce>2.0.co;2

Bechtold, P., Koehler, M., Jung, T., Doblas-Reyes, F., Leutbecher, M., Rodwell, M. J., et al. (2008). Advances in simulating atmospheric variability with the ECMWF model: From synoptic to decadal time-scales. *Quarterly Journal of the Royal Meteorological Society*, *134*(634), 1337–1351. https://doi.org/10.1002/qj.289

Betts, A. K. (1975). Parametric interpretation of trade-wind cumulus budget studies. *Journal of the Atmospheric Sciences*, *32*(10), 1934–1945. https://doi.org/10.1175/1520-0469(1975)032<1934:piotwc>2.0.co;2

Böing, S. J., Siebesma, A. P., Korpershoek, J. D., & Jonker, H. J. (2012). Detrainment in deep convection. *Geophysical Research Letters*, *39*(20), 20816. https://doi.org/10.1029/2012GL053735

Brown, A., Cederwall, R., Chlond, A., Duynkerke, P., Golaz, J.-C., Khairoutdinov, M., et al. (2002). Large-eddy simulation of the diurnal cycle of shallow cumulus convection over land. *Quarterly Journal of the Royal Meteorological Society*, *128*(582), 1075–1093. https://doi.org/10.1256/003590002320373210

Byers, H. R., & Braham, R. R. (1949). *The thunderstorm: Report of the thunderstorm project*. US Government Printing Office.

Carpenter, R., Droegemeier, K., & Blyth, A. M. (1998). Entrainment and detrainment in numerically simulated cumulus congestus clouds. Part II: Cloud budgets. *Journal of the Atmospheric Sciences*, *55*(23), 3433–3439. https://doi.org/10.1175/1520-0469(1998)055h3433:EADINSi2.0.CO;2

Casey, S. P. F., Fetzer, E. J., & Kahn, B. H. (2012). Revised identification of tropical oceanic cumulus congestus as viewed by CloudSat. *Atmospheric Chemistry and Physics*, *12*(3), 1587–1595. https://doi.org/10.5194/acp-12-1587-2012

Davies, L., Jakob, C., May, P., Kumar, V. V., & Xie, S. (2013). Relationships between the large-scale atmosphere and the small-scale convective state for Darwin, Australia. *Journal of Geophysical Research: Atmospheres*, *118*(20), 11534–11545. https://doi.org/10.1002/jgrd.50645

Dee, D. P., Uppala, S. M., Simmons, A. J., Berrisford, P., Poli, P., Kobayashi, S., et al. (2011). The ERA-Interim reanalysis: Configuration and performance of the data assimilation system. *Quarterly Journal of the Royal Meteorological Society*, *137*(656), 553–597. https://doi.org/10.1002/qj.828

de Rooy, W. C., Bechtold, P., Fröhlich, K., Hohenegger, C., Jonker, H., Mironov, D., et al. (2012). Entrainment and detrainment in cumulus convection: An overview. *Quarterly Journal of the Royal Meteorological Society*, *139*(670), 1–19. https://doi.org/10.1002/qj.1959

de Rooy, W. C., & Siebesma, A. (2010). Analytical expressions for entrainment and detrainment in cumulus convection. *Quarterly Journal of the Royal Meteorological Society*, *136*(650), 1216–1227. https://doi.org/10.1002/qj.640

de Rooy, W. C., Siebesma, A. P., de Rooy, W. C., & Siebesma, A. P. (2008). A simple parameterization for detrainment in shallow cumulus. *Monthly Weather Review*, *136*(2), 560–576. https://doi.org/10.1175/2007MWR2201.1

Emanuel, K. A., David Neelin, J., & Bretherton, C. S. (1994). On large-scale circulations in convecting atmospheres. *Quarterly Journal of the Royal Meteorological Society*, *120*(519), 1111–1143. https://doi.org/10.1002/qj.49712051902

Giangrande, S. E., Collis, S., Straka, J., Protat, A., Williams, C., & Krueger, S. (2013). A summary of convective-core vertical velocity properties using ARM UHF wind profilers in Oklahoma. *Journal of Applied Meteorology and Climatology*, *52*(10), 2278–2295. https://doi.org/10.1175/JAMC-D-12-0185.1

Giangrande, S. E., Toto, T., Jensen, M. P., Bartholomew, M. J., Feng, Z., Protat, A., et al. (2016). Convective cloud vertical velocity and mass-flux characteristics from radar wind profiler observations during GoAmazon2014/5. *Journal of Geophysical Research: Atmospheres*, *121*(21), 12891–12913. https://doi.org/10.1002/2016JD025303

Gregory, D., & Rowntree, P. R. (1990). A mass flux convection scheme with representation of cloud ensemble characteristics and stability-dependent closure. *Monthly Weather Review*, *118*(7), 1483–1506. https://doi.org/10.1175/1520-0493(1990)118<1483:amfcsw>2.0.co;2

Houze, R. A., Rasmussen, K. L., Zuluaga, M. D., & Brodzik, S. R. (2015). The variable nature of convection in the tropics and subtropics: A legacy of 16 years of the tropical rainfall measuring mission satellite. *Reviews of Geophysics*, *53*(3), 994–1021. https://doi.org/10.1002/2015rg000488

Jackson, R. C., Collis, S. M., Louf, V., Protat, A., & Majewski, L. (2018). A 17 year climatology of the macrophysical properties of convection in Darwin. *Atmospheric Chemistry and Physics*, *18*(23), 17687–17704. https://doi.org/10.5194/acp-18-17687-2018

Jakob, C. (2010). Accelerating progress in global atmospheric model development through improved parameterizations: Challenges, opportunities, and strategies. *Bulletin of the American Meteorological Society*, *91*(7), 869–875. https://doi.org/10.1175/2009BAMS2898.1

Jeyaratnam, J., Luo, Z. J., Giangrande, S. E., Wang, D., & Masunaga, H. (2021). A satellite-based estimate of convective vertical velocity and convective mass flux: Global survey and comparison with radar wind profiler observations. *Geophysical Research Letters*, *48*(1), e2020GL090675. https://doi.org/10.1029/2020gl090675

Keenan, T., Glasson, K., Cummings, F., Bird, T. S., Keeler, J., Lutz, J., et al. (1998). The BMRC/NCAR C-band polarimetric (C-POL) radar system. *Journal of Atmospheric and Oceanic Technology*, *15*(4), 871–886. https://doi.org/10.1175/1520-0426(1998)015<0871:tbncbp>2.0.co;2

Kumar, V. V., Jakob, C., Protat, A., May, P. T., & Davies, L. (2013). The four cumulus cloud modes and their progression during rainfall events: A C-band polarimetric radar perspective. *Journal of Geophysical Research: Atmospheres*, *118*(15), 8375–8389. https://doi.org/10.1002/jgrd.50640

Kumar, V. V., Jakob, C., Protat, A., May, P. T., & Williams, C. R. (2015). Mass-flux characteristics of tropical cumulus clouds from wind profiler observations at Darwin, Australia. *Journal of the Atmospheric Sciences*, *72*(5), 1837–1855. https://doi.org/10.1175/jas-d-14-0259.1

Kumar, V. V., Protat, A., Jakob, C., Williams, C. R., Rauniyar, S., Stephens, G. L., & May, P. T. (2016). The estimation of convective mass flux from radar reflectivities. *Journal of Applied Meteorology and Climatology*, *55*(5), 1239–1257. https://doi.org/10.1175/JAMC-D-15-0193.1

Kumar, V. V., Protat, A., May, P. T., Jakob, C., Penide, G., Kumar, S., & Davies, L. (2013). On the effects of large-scale environment and surface types on convective cloud characteristics over Darwin, Australia. *Monthly Weather Review*, *141*(4), 1358–1374. https://doi.org/10.1175/mwr-d-12-00160.1

Kummerow, C., Barnes, W., Kozu, T., Shiue, J., & Simpson, J. (1998). The tropical rainfall measuring mission (TRMM) sensor package. *Journal of Atmospheric and Oceanic Technology*, *15*, 809–817. https://doi.org/10.1175/1520-0426(1998)015<0809:ttrmmt>2.0.co;2

Labbouz, L., Kipling, Z., Stier, P., Protat, A., Labbouz, L., Kipling, Z., et al. (2018). How well can we represent the spectrum of convective clouds in a climate model? Comparisons between internal parameterization variables and radar observations. *Journal of the Atmospheric Sciences*, *75*(5), 1509–1524. https://doi.org/10.1175/JAS-D-17-0191.1

LeMone, M. A., & Zipser, E. J. (1980). Cumulonimbus vertical velocity events in GATE. Part I: Diameter, intensity and mass flux. *Journal of the Atmospheric Sciences*, *37*(11), 2444–2457. https://doi.org/10.1175/1520-0469(1980)037<2444:CVVEIG>2.0.CO;2

Lin, C., Arakawa, A. (1997). The macroscopic entrainment processes of simulated cumulus ensemble. Part II: Testing the entraining-plume model. *Journal of the Atmospheric Sciences*, *54*(8), 1044–1053. https://doi.org/10.1175/1520-0469(1997)054<1044:TMEPOS>2.0.CO;2

Louf, V., Jakob, C., Protat, A., Bergemann, M., & Narsey, S. (2019). The relationship of cloud number and size with their large-scale environment in deep tropical convection. *Geophysical Research Letters*, *46*(15), 9203–9212. https://doi.org/10.1029/2019gl083964

Marwitz, J. D. (1973). Trajectories within the weak echo regions of hailstorms. *Journal of Applied Meteorology and Climatology*, *12*(7), 1174–1182. https://doi.org/10.1175/1520-0450(1973)012<1174:TWTWER>2.0.CO;2

Masunaga, H., & Luo, Z. J. (2016). Convective and large-scale mass flux profiles over tropical oceans determined from synergistic analysis of a suite of satellite observations. *Journal of Geophysical Research: Atmospheres*, *121*(13), 7958–7974. https://doi.org/10.1002/2016JD024753

May, P. T., Mather, J. H., Vaughan, G., Jakob, C., McFarquhar, G. M., Bower, K. N., & Mace, G. G. (2008). The tropical warm pool international cloud experiment. *Bulletin of the American Meteorological Society*. https://doi.org/10.1175/BAMS-89-5-629

Neale, R. B., Chen, C.-C., Gettelman, A., Lauritzen, P. H., Park, S., Williamson, D. L., et al. (2010). Description of the NCAR community atmosphere model (CAM 5.0). *NCAR Technical Note NCAR/TN-486+ STR*, *1*(1), 1–12.

Nesbitt, S. W., Zipser, E. J., & Cecil, D. J. (2000). A census of precipitation features in the tropics using TRMM: Radar, ice scattering, and lightning observations. *Journal of Climate*, *13*, 4087–4106. https://doi.org/10.1175/1520-0442(2000)013<4087:acopfi>2.0.co;2

Nitta, T. (1975). Observational determination of cloud mass flux distributions. *Journal of the Atmospheric Sciences*, *32*(1), 73–91. https://doi.org/10.1175/1520-0469(1975)032<0073:odocmf>2.0.co;2

Nitta, T., & Esbensen, S. K. (1974). Heat and moisture budget analyses using BOMEX data. *Monthly Weather Review*, *102*, 17–28. https://doi.org/10.1175/1520-0493(1974)102<0017:hambau>2.0.co;2

Oerlemans, J. (1986). Convection in a conditionally unstable atmosphere: A re-investigation of BJERKNES' slice method. *Contributions to Atmospheric Physics*, *59*, 41–53.

Ooyama, K. (1971). A theory on parameterization of cumulus convection. *Journal of the Meteorological Society of Japan. Ser. II*, *49A*(0), 744–756. https://doi.org/10.2151/jmsj1965.49a.0_744

Peters, K., Crueger, T., Jakob, C., & Möbis, B. (2017). Improved MJO-simulation in ECHAM6.3 by coupling a Stochastic Multicloud Model to the convection scheme. *Journal of Advances in Modeling Earth Systems*, *9*(1), 193–219. https://doi.org/10.1002/2016MS000809

Peters, K., Jakob, C., & Davies, L. (2013). Stochastic behavior of tropical convection in observations and a multicloud model. *Journal of the Atmospheric Sciences*, *70*(11), 3556–3575. https://doi.org/10.1175/jas-d-13-031.1

Riehl, H., & Malkus, J. S. (1958). On the heat balance in the equatorial trough zone. *Geophysica*, *6*, 503–538.

Riehl, H., & Malkus, J. S. (1979). The heat balance of the equatorial trough zone, revisited. *Contributions to Atmospheric Physics*, *52*, 287–305.

Romps, D. M. (2010). A direct measure of entrainment. *Journal of the Atmospheric Sciences*, *67*(6), 1908–1927. https://doi.org/10.1175/2010jas3371.1

Schalkwijk, J., Jonker, H. J. J., Siebesma, A. P., & Bosveld, F. C. (2015). A year-long large-eddy simulation of the weather over Cabauw: An overview. *Monthly Weather Review*, *143*(3), 828–844. https://doi.org/10.1175/MWR-D-14-00293.1

Schemann, V., Ebell, K., Pospichal, B., Neggers, R., Moseley, C., & Stevens, B. (2020). Linking large-eddy simulations to local cloud observations. *Journal of Advances in Modeling Earth Systems*, *12*(12), e2020MS002209. https://doi.org/10.1029/2020MS002209

Schiro, K. A., Ahmed, F., Giangrande, S. E., & Neelin, J. D. (2018). GoAmazon2014/5 campaign points to deep-inflow approach to deep convection across scales. *Proceedings of the National Academy of Sciences of the United States of America*, *115*(18), 4577–4582. https://doi.org/10.1073/pnas.1719842115

Schumacher, C., & Houze, R. A. (2003). *Stratiform rain in the tropics as seen by the TRMM precipitation radar* (Vol. 16, Technical Report No. 11).Retrieved from http://daac.gsfc.nasa.gov/

Siebesma, A. P. (1996). *On the mass flux approach for atmospheric convection*. ECMWF. Retrieved from https://www.ecmwf.int/node/12223

Siebesma, A. P., Bony, S., Jakob, c., & Stevens, B. (2020). Parameterising clouds. In *Clouds and climate: Climate science's greatest challenge* (pp. 170–217). Cambridge University Press. https://doi.org/10.1017/9781107447738.007

Siebesma, A. P., Bretherton, C. S., Brown, A., Chlond, A., Cuxart, J., Duynkerke, P. G., et al. (2003). A large eddy simulation intercomparison study of shallow cumulus convection. *Journal of the Atmospheric Sciences*, *60*(10), 1201–1219. https://doi.org/10.1175/1520-0469(2003)60<1201:alesis>2.0.co;2

Siebesma, A. P., Cuijpers, J. W. M., Siebesma, A. P., & Cuijpers, J. W. M. (1996). Evaluation of parametric assumptions for shallow cumulus convection. *Journal of the Atmospheric Sciences*, *52*(6), 650–666. https://doi.org/10.1175/1520-0469(1995)052<0650:eopafs>2.0.co;2

Simpson, J., Halverson, J. B., Ferrier, B. S., Petersen, W. A., Simpson, R. H., Blakeslee, R., & Durden, S. L. (1998). On the role of "hot towers" in tropical cyclone formation. *Meteorology and Atmospheric Physics*, *67*(1–4), 15–35. https://doi.org/10.1007/BF01277500

Steiner, M., Houze, R. A., & Yuter, S. E. (1995). Climatological characterization of three-dimensional storm structure from operational radar and rain gauge data. *Journal of Applied Meteorology*, *34*(9), 1978–2007. https://doi.org/10.1175/1520-0450(1995)034<1978:ccotds>2.0.co;2

Stephens, G. L., Vane, D. G., Boain, R. J., Mace, G. G., Sassen, K., Wang, Z., et al. (2002). The CloudSat mission and the A-Train: A new dimension of space-based observations of clouds and precipitation. *Bulletin of the American Meteorological Society*, *83*(12), 1771–1790. https://doi.org/10.1175/bams-83-12-1771

Tiedtke, M. (1989). A comprehensive mass flux scheme for cumulus parameterization in large-scale models. *Monthly Weather Review*, *117*(8), 1779–1880. https://doi.org/10.1175/1520-0493(1989)117<1779:acmfsf>2.0.co;2

VanZanten, M. C., Stevens, B., Nuijens, L., Siebesma, A. P., Ackerman, A., Burnet, F., et al. (2011). Controls on precipitation and cloudiness in simulations of trade-wind cumulus as observed during RICO. *Journal of Advances in Modeling Earth Systems*, *3*(2). https://doi.org/10.1029/2011ms000056

Wagner, T. M., & Graf, H. F. (2010). An ensemble cumulus convection parameterization with explicit cloud treatment. *Journal of the Atmospheric Sciences*. https://doi.org/10.1175/2010JAS3485.1

Wang, J., Fan, J., Houze, R. A., Jr., Brodzik, S. R., Zhang, K., Zhang, G. J., & Ma, P.-L. (2021). Using radar observations to evaluate 3-D radar echo structure simulated by the Energy Exascale Earth System Model (E3SM) version 1. *Geoscientific Model Development*, *14*(2), 719–734. https://doi.org/10.5194/gmd-14-719-2021

Wang, M., & Zhang, G. J. (2018). Improving the simulation of tropical convective cloud-top heights in CAM5 with CloudSat observations. *Journal of Climate*, *31*(13), 5189–5204. https://doi.org/10.1175/jcli-d-18-0027.1

Williams, C. R. (2012). Vertical air motion retrieved from dual-frequency profiler observations. *Journal of Atmospheric and Oceanic Technology*, *29*(10), 1471–1480. https://doi.org/10.1175/JTECH-D-11-00176.1

Yanai, M., Esbensen, S., Chu, J.-H., Yanai, M., Esbensen, S., & Chu, J.-H. (1973). Determination of bulk properties of tropical cloud clusters from large-scale heat and moisture budgets. *Journal of the Atmospheric Sciences*, *30*(4), 611–627. https://doi.org/10.1175/1520-0469(1973)030<0611:DOBPOT>2.0.CO;2

Zhang, M. H., & Lin, J. L. (1997). Constrained variational analysis of sounding data based on column-integrated budgets of mass, heat, moisture, and momentum: Approach and application to ARM measurements. *Journal of the Atmospheric Sciences*, *54*(11), 1503–1524. https://doi.org/10.1175/1520-0469(1997)054<1503:cvaosd>2.0.co;2

Zipser, E. J. (2003). Some views on "hot towers" after 50 years of tropical field programs and two years of TRMM data. In W.-K. Tao & R. Adler (Eds.), *Cloud systems, hurricanes, and the tropical rainfall measuring mission (TRMM): A tribute to Dr. Joanne Simpson* (pp. 49–58). American Meteorological Society. https://doi.org/10.1007/978-1-878220-63-9_5